Nanoscale Advances

ROYAL SOCIETY OF CHEMISTRY

PAPER

View Article Online
View Journal | View Issue

Cite this: *Nanoscale Adv.*, 2021, **3**, 3216

$NiCo_2O_4$ nanoparticles inlaid on sulphur and nitrogen doped and co-doped rGO sheets as efficient electrocatalysts for the oxygen evolution and methanol oxidation reactions†

Rebekah, C. Viswanathan and N. Ponpandian *

The present work depicts the fabrication of $NiCo_2O_4$ decorated on rGO, and doped and co-doped rGO and its electrocatalytic activity towards the oxygen evolution reaction and methanol oxidation reaction. The $NiCo_2O_4$ catalyst with S-doped rGO outperformed the other catalysts, indicating that the sulphur atoms attached on rGO possess low oxophilicity and optimum free energy. This results in facile adsorption of the intermediate products formed during the OER and a rapid release of O_2 molecules. The same catalyst requires an overpotential of 1.51 V *vs.* RHE to attain the benchmark current density value of 10 mA cm^{-2} and shows a Tafel slope of 57 mV dec^{-1}. It also reveals outstanding stability during its operation for 10 h with a minimum loss in potential. On the other hand, $NiCo_2O_4$/S,N-rGO reveals superior activity with high efficiency and stability in catalyzing methanol oxidation. The catalyst delivered a low onset potential of 0.12 V *vs.* Hg/HgO and high current density of 203.4 mA cm^{-2} after addition of 0.5 M methanol, revealing the outstanding performance of the electrocatalyst.

Received 19th February 2021
Accepted 28th March 2021

DOI: 10.1039/d1na00135c

rsc.li/nanoscale-advances

1 Introduction

Energy production from conventional fossil fuels results in the release of large quantities of carbon and other poisonous gases.[1] This greatly influences the flora and fauna of the planet which leads to the urgency in developing a clean energy source from intermittent renewable energy resources. Energy production from such resources requires efficient energy conversion and storage devices. Hydrogen has emerged as a clean source of energy which is abundantly available in nature.[2] Nowadays, water electrolysis is considered as a feasible technique for production of hydrogen, which is regarded to be a clean energy carrier having high energy density. Electrochemically splitting water into O_2 and H_2 gases takes place *via* the oxygen evolution reaction (OER) at the anode and the hydrogen evolution reaction (HER) at the cathode. This half cell reaction can be effectively stimulated by effective electrocatalysts which is a prerequisite for overall performance of water electrolysis. However, fabricating electrocatalysts for driving the OER is of utmost importance as it is a multiple electron–proton transfer process. To date, IrO_2 and RuO_2 based electrocatalysts have proven to be efficient electrocatalysts for the OER. However, certain drawbacks such as poor stability and scarcity greatly hinder their use in practical applications.[3–7] In addition, fuel cells generate electricity by employing hydrogen as a fuel. In the same manner, direct methanol fuel cells (DMFCs) also produce electricity by oxidizing methanol fuel applied at the anode to H_2 which is a tedious multi-step process. Pt, Ru and Pd based electrocatalysts were accepted as superior electrocatalysts, but they suffered from certain drawbacks and limitations which impeded the commercialization of DMFCs. Therefore, designing and exploring high-performance electrocatalysts with low cost and abundant reserves for the methanol oxidation reaction (MOR) has attracted much interest and still remains a great challenge.[8–11] Recently, mixed transition metal (spinel oxide) based catalysts have attracted enormous interest due to their easy synthesis, low cost, abundance and the existence of more valence states.[12–15] $NiCo_2O_4$ has emerged as a potential electrocatalyst because it shows excellent redox behaviour, easily penetrates through the electrolyte and has relatively lower resistance to the diffusion of protons/cations.[16,17] Various studies have been reported so far based on $NiCo_2O_4$ and its composites with carbon based materials and they are summarized in Table 2. But the major drawback of this material is poor conductivity of electrons which hinders its application in the field of electrocatalysis such as the OER, ORR and HER. To improve the conductivity of such materials and suppress the aggregation of nanostructures occurring due to a greater number of oxidation states, spinel oxides were intercalated with a few carbon materials such as reduced graphene oxide (rGO), carbon

Department of Nanoscience and Technology, Bharathiar University, Coimbatore-641046, India. E-mail: ponpandian@buc.edu.in; Fax: +91-422-2422-387; Tel: +91-422-2428-421

† Electronic supplementary information (ESI) available. See DOI: 10.1039/d1na00135c

nanofibers (CNF) and carbon nanotubes (CNT).[18–22] In this work, rGO is incorporated as a carbon substrate due to its outstanding properties such as large surface area, existence of a greater number of active surface sites, and presence of epoxy and carbonyl functional groups at the edges of the sheet. These properties enable it to be a superior carbon support by efficiently conducting electrons, and the oxygenated functional groups serve as an anchoring site for adsorption of intermediate products. In addition, doping and co-doping with heteroatoms also significantly improves the electronic properties by replacing the carbon atoms in the graphitic structure. This creates defects in the adjacent sites due to the varying bond length and size of the atom.[23] As a result, uneven charge distribution arises due to the difference in size and electronegativity of the heteroatoms compared with those of carbon atoms. Nevertheless, due to the incorporated heteroatoms having electronegativity higher (as in the case of N) or lower (as in the case of S) than that of carbon, there occurs an electron modulation to change the charge distribution in the carbon network. This increases the interaction with the reactants to offer active sites for catalytic OER application.[24–27] In the same manner, co-doping of heteroatoms into a carbon network further improves the electrocatalytic performance due to its difference in electronegativity and oxophilicity of heteroatoms. Moni *et al.* investigated the OER catalytic performance using a $NiCo_2O_4$–nitrogen doped graphene oxide composite which required a low overpotential of 1.63 V to achieve a current density of 10 mA cm^{-2}.[28] Liu *et al.* found that $NiCo_2O_4$ with a combination of defect-rich and ultrathin structure revealed outstanding OER performance for Zn–air batteries.[29] Li *et al.* reported that $NiCo_2O_4$ 3-D nanoflowers supported on graphene nanosheets (GNs) exhibit favorable catalytic performance with a low onset potential (1.50 V), a small Tafel slope (137 mV dec^{-1}) and good stability toward the OER.[21]

In the present work, we have prepared pristine $NiCo_2O_4$, $NiCo_2O_4$/rGO, $NiCo_2O_4$/S-rGO, and $NiCo_2O_4$/S,N-rGO composites and their electrocatalytic performance towards the OER was evaluated. Spinel $NiCo_2O_4$ is coupled with rGO to enhance the electron transport and to prevent the agglomeration of nanostructures which helps in improving the electrocatalytic performance. In addition, rGO was doped with S heteroatoms and co-doped with S & N heteroatoms, which also significantly improved the OER catalysis. $NiCo_2O_4$/S-rGO outperformed all the other catalysts in alkaline medium, requiring a low overpotential (280 mV) to achieve a current density of 10 mA cm^{-2} and exhibiting a small Tafel slope (57 mV dec^{-1}).

2 Experimental methods

2.1 Chemicals and materials

Cobalt(II) acetate tetrahydrate (GRM 1359), nickel(II) acetate tetrahydrate (GRM 6100), graphite flakes, potassium permanganate ($KMnO_4$), sodium meta-bisulfite, thiourea, sodium nitrate and CTAB were bought from Hi-Media Laboratory Pvt. Ltd, Mumbai, India. H_2O_2, HCl and conc. H_2SO_4 were bought from Sigma-Aldrich (Merck).

2.2 Synthesis of pristine $NiCo_2O_4$

Pristine $NiCo_2O_4$ nanostructures were prepared using a hydrothermal process as described in previously reported literature with a minor modification.[30,31] In brief, 1 M Ni(Ac) and 2 M Co(Ac) were mixed together by stirring magnetically in 30 mL of distilled water (DW). To this solution, 2 mM CTAB was added, and the mixture was allowed to stir for 2 h and then transferred to an autoclave, which was placed in a hot air oven and maintained at 200 °C for 12 h. The treated product was cleaned and dried at 60 °C till a dried powder was obtained. Then, the obtained powder was annealed at 600 °C for 2 h and the final product was denoted as pristine $NiCo_2O_4$ nanostructures.

2.3 Synthesis of the $NiCo_2O_4$/rGO nanocomposite

The $NiCo_2O_4$/rGO nanocomposite was synthesized using a facile hydrothermal method. In the synthesis process, 0.1 M nickel acetate and 0.2 M cobalt acetate were dispersed in 20 mL of DW and allowed to stir for 3 h till the attainment of a transparent solution. To the above solution, the required amount of CTAB was added as a surfactant and simultaneously 50 mg of GO exfoliated by water bath sonication was poured into it. GO was obtained from graphite flakes by exfoliating it in strong acids (modified Hummers method) which is reported in our earlier work.[32,33] The mixture was then sealed in a Teflon-lined autoclave and hydrothermally treated at 180 °C for 15 h. The treated mixture was washed to remove the unreacted particles existing in the mixture. It was then dried and calcined in an Ar atmosphere at 350 °C with a heating rate of 5° min^{-1} to obtain a spinel $NiCo_2O_4$/rGO composite.

2.4 Synthesis of the $NiCo_2O_4$/heteroatom doped rGO nanocomposite

The preparation protocol of the $NiCo_2O_4$/heteroatom doped rGO nanocomposite is presented schematically in Scheme 1. In the synthesis protocol, initially 50 mg of GO was exfoliated by sonication for 3 h till the obtainment of a homogeneous dispersion. To the GO solution, an appropriate amount of the dopant precursor was also added to the same solution. Sodium meta-bisulfite ($Na_2S_2O_5$) was used as a precursor for S-doping and thiourea for S and N co-doping. After adding dopant precursors, the mixture was stirred for 2 h and then treated hydrothermally at 150 °C for 8 h. The obtained product was finally calcined in an inert atmosphere at 350 °C for doping of heteroatoms on the carbon network. The sodium meta-bisulfite added sample was denoted as S doped rGO and the thiourea added sample was denoted as S and N co-doped rGO. For the preparation of the $NiCo_2O_4$/heteroatom doped rGO nanocomposite, 100 mg of the prepared $NiCo_2O_4$ nanostructures was intercalated with 30 mg of heteroatom doped rGO by stirring and thermally treated at 60 °C for 5 h. Then it was allowed to settle down and finally washed with water and ethanol. The obtained samples were denoted as $NiCo_2O_4$/S-rGO and $NiCo_2O_4$/S,N-rGO nanocomposites.

2.5 Materials characterization

X-ray Diffraction (XRD) analysis was done using an XRD Rigaku Ultima IV X-ray diffractometer (Cu-Kα1 radiation, $\lambda = 1.5406$ Å)

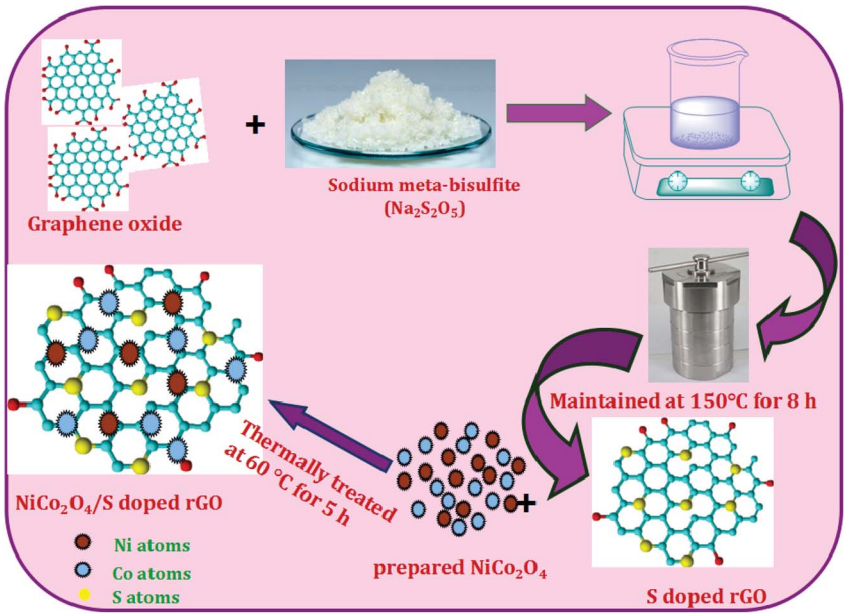

Scheme 1 Schematic representation of $NiCo_2O_4$/S-rGO composite preparation.

to confirm the phase formation and purity of the samples. The morphological analysis was done using FESEM (FEI, QUANTA 250-FEG, Germany) and the composition of elements present in the samples was analyzed using EDAX (Bruker, Germany) combined with FESEM. The functional group analysis was performed using FTIR (Jasco Tensor 27, Japan). XPS (PHI VersaProbe III, Japan) analysis was done to investigate the various oxidation states existing in the samples.

2.6 Electrochemical measurements

The OER electrocatalytic performance of the synthesized samples was investigated using a PARSTAT analytical electrochemical workstation consisting of a standard three electrode system. As a working electrode, a glassy carbon electrode (GCE) coated with the samples was used, and platinum wire and Hg/HgO were employed as the counter electrode and reference electrode, respectively. Initially, before modifying the GCE with the catalyst, it was cleaned by polishing with alumina powder of various sizes (1.0, 0.3 and 0.05 μm) and washed by sonication in a mixture of ethanol and DW till a mirror-like surface was obtained. For slurry preparation, 5 mg of catalysts (pristine $NiCo_2O_4$, $NiCo_2O_4$/rGO, $NiCo_2O_4$/S-rGO and $NiCo_2O_4$/S,N-rGO) was added to a mixture of ethanol (20 μL) and Nafion (5 μL, DuPont, 0.5 wt%) and dispersed by sonication for 1 h. 5 μL of the dispersed solution/slurry was pipetted and coated on the GCE surface. Then it was allowed to dry at ambient temperature and used for further investigations. The electrocatalysis towards the OER was demonstrated in 1 M KOH under an O_2 saturated atmosphere. The polarization plot was recorded at a sweep rate of 5 mV s^{-1} from which the overpotential required to deliver a current density of 10 mA cm^{-2} and the onset potential at which evolution of oxygen begins is calculated. In order to understand the OER kinetics, Tafel plots were fitted by re-plotting the polarization curves. All the measurements recorded during the catalytic OER w.r.t Hg/HgO were converted to the reversible hydrogen electrode (RHE) scale using the Nernst equation

$$E_{RHE} = E_{Hg/HgO} + E^{\circ}_{Hg/HgO} + 0.059 \times pH \quad (1)$$

The stability of the catalysts was demonstrated using the chronoamperometry (CA) technique at a stable potential of 1.54 V *vs.* RHE for durations of 1000 s and 10 000 s. Stability was also further evaluated using the chronopotentiometry technique at

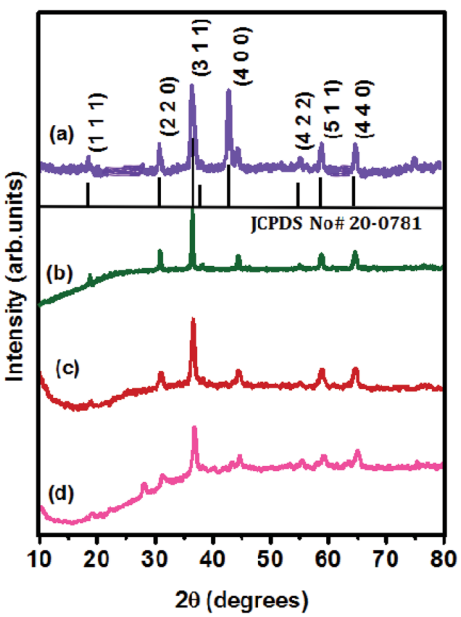

Fig. 1 XRD patterns of (a) pristine $NiCo_2O_4$, (b) $NiCo_2O_4$/rGO, (c) $NiCo_2O_4$/S-rGO, and (d) $NiCo_2O_4$/S,N-rGO.

a constant current density of 10 mA cm^{-2} for a time period of 10 h. The charge transfer ability of the electrocatalyst was assessed using electrochemical impedance spectroscopy (EIS) which was conducted in the frequency range from 10 kHz to 0.1 Hz with an amplitude of 0.02 V. The electrochemically active surface area (ECSA) was derived from the fraction of double layer capacitance value (C_{dl}) calculated from CV curves recorded in the non-faradaic potential region (0.5 to 0.6 V *vs.* RHE) at different scan rates (20–180 mV s^{-1}) and specific capacitance of the electrode surface (C_s).

3 Results and discussion

3.1 Structural and functional group analysis

Structural analysis of the synthesized products was performed using XRD and the patterns are displayed in Fig. 1. The XRD pattern of pristine $NiCo_2O_4$ presented in Fig. 1(a) contains obvious diffraction peaks at 18.78, 31.8, 37, 44.1, 54.6, 59.1 and 64.9°, which were ascribed to the (1 1 1), (2 2 0), (3 1 1), (4 0 0), (4 2 2), (5 1 1) and (4 4 0) planes and matched well with the JCPDS card no: 20-0781. The diffraction pattern also clearly revealed the formation of a cubic spinel phase with the space group *F*3*dm*, and the absence of additional peaks confirmed that the samples were highly crystalline in nature. All the XRD patterns of the $NiCo_2O_4$/rGO, $NiCo_2O_4$/S-rGO and $NiCo_2O_4$/S,N-rGO samples shown in Fig. 1(b)–(d) also exhibit the spinel phase, and the weak peak observed at around 26° confirms that GO was reduced during hydrothermal treatment.[21] In Fig. 1(c), it was perceived that the characteristic diffraction peak of rGO at around $2\theta = 26°$ was suppressed which might be due to the disordered structure and poor intensity of diffraction.[32,34] In the XRD pattern of $NiCo_2O_4$/S,N-rGO depicted in Fig. 1(d), the intensity of diffraction peaks is highly reduced and the

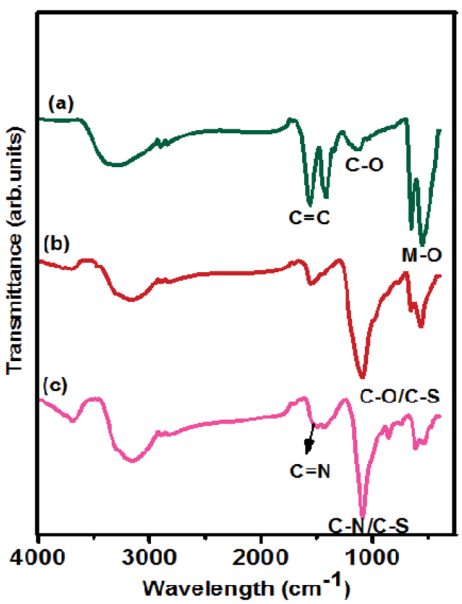

Fig. 2 FTIR spectra of (a) $NiCo_2O_4$/rGO, (b) $NiCo_2O_4$/S-rGO, and (c) $NiCo_2O_4$/S,N-rGO.

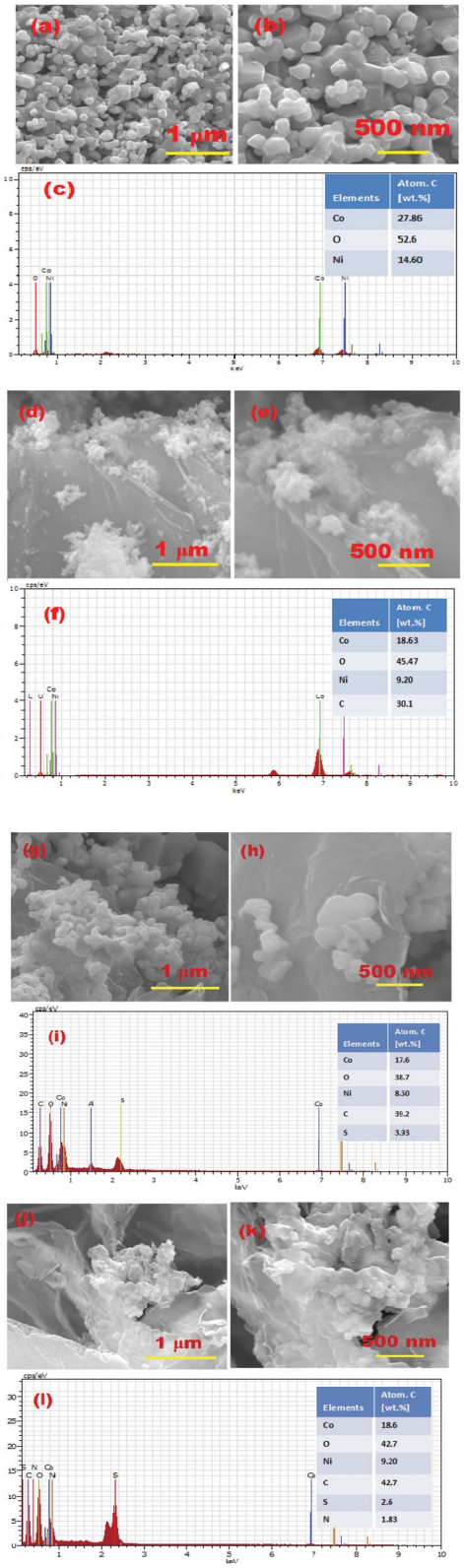

Fig. 3 (a and b) FESEM images of pristine $NiCo_2O_4$, (c) EDX spectrum of pristine $NiCo_2O_4$, (d and e) FESEM images of $NiCo_2O_4$/rGO, (f) EDX spectrum of $NiCo_2O_4$/rGO, (g and h) FESEM images of $NiCo_2O_4$/S-rGO, (i) EDX spectrum of $NiCo_2O_4$/S-rGO, (j and k) FESEM images of $NiCo_2O_4$/S,N-rGO and (l) EDX spectrum of $NiCo_2O_4$/S,N-rGO.

existence of an obvious peak at 26° was noticed. This might be due to co-doping of heteroatoms in the carbon network.

Also, heteroatom doping and co-doping didn't alter the crystal structure which further proves that heteroatoms have been perfectly doped into the carbon network by replacing carbon atoms. The crystallite size of the $NiCo_2O_4$/S-rGO nanocomposite was calculated using the Scherrer formula, $D = 0.9\lambda/\beta \cos\theta$, and it was found to be 18 nm.

Functional group analysis of the prepared catalysts was performed using FTIR and the corresponding spectra are shown in Fig. 2. The FTIR spectrum of $NiCo_2O_4$/rGO is displayed in Fig. 2(a) in which the characteristic band noticed at 562 cm^{-1} was ascribed to the metal oxide bond located at the tetrahedral site and that at 660 cm^{-1} was ascribed to the metal oxide bond at the octahedral site of the $NiCo_2O_4$ spinel structure.[35] The strong peaks observed at 1566, 1416 and 1145 cm^{-1} were attributed to the vibrational modes of C=C, O=C–C and C–O bonds, respectively. In the FTIR spectrum of $NiCo_2O_4$/S-rGO shown in Fig. 2(b), the major peaks observed at 1091, 1511, 1443 and 856 cm^{-1} were attributed to C–S, C=C, O=C–C and C–S,[36] which clearly established that S was successfully doped on rGO sheets by replacing carbon atoms from the appropriate positions. Similarly, in the spectrum of $NiCo_2O_4$/S,N-rGO which is shown in Fig. 2(c), the absorption band at 1538 cm^{-1} was attributed to the vibrational mode of C=N and the peak observed at 1086 cm^{-1} is due to the bonding of sulphur and nitrogen with the carbon atoms.[37]

3.2 Elemental and morphological analysis

The surface morphology and compositional analysis of the prepared catalysts was performed using field emission scanning electron microscopy and EDX. The micrographs were recorded at a scan rate of 90 μS and an applied potential of 20 kV. Fig. 3 shows the micrographs of pristine $NiCo_2O_4$, $NiCo_2O_4$/rGO, $NiCo_2O_4$/S-rGO and $NiCo_2O_4$/S,N-rGO. Fig. 3(a and b) show the FESEM images of pristine $NiCo_2O_4$, which exhibits a hexagonal shape with the average diameter ranging from 350 to 500 nm. The nanostructures were formed by the aggregation of flake-like structures during hydrothermal treatment in which the hydroxide ions along with metal ions contributed to the development of nuclei formation and finally resulted in the growth of hexagonal nanostructures. Fig. 3(c) shows the corresponding EDX spectrum from which the purity of the sample was confirmed. Fig. 3(d and e) show the FESEM images of $NiCo_2O_4$/rGO, Fig. 3(g and h) show the FESEM micrographs of $NiCo_2O_4$/S-rGO, and Fig. 3(j and k) show the micrographs of the $NiCo_2O_4$/S,N-rGO nanocomposite. It was observed that in all the composite samples, $NiCo_2O_4$ nanostructures were firmly

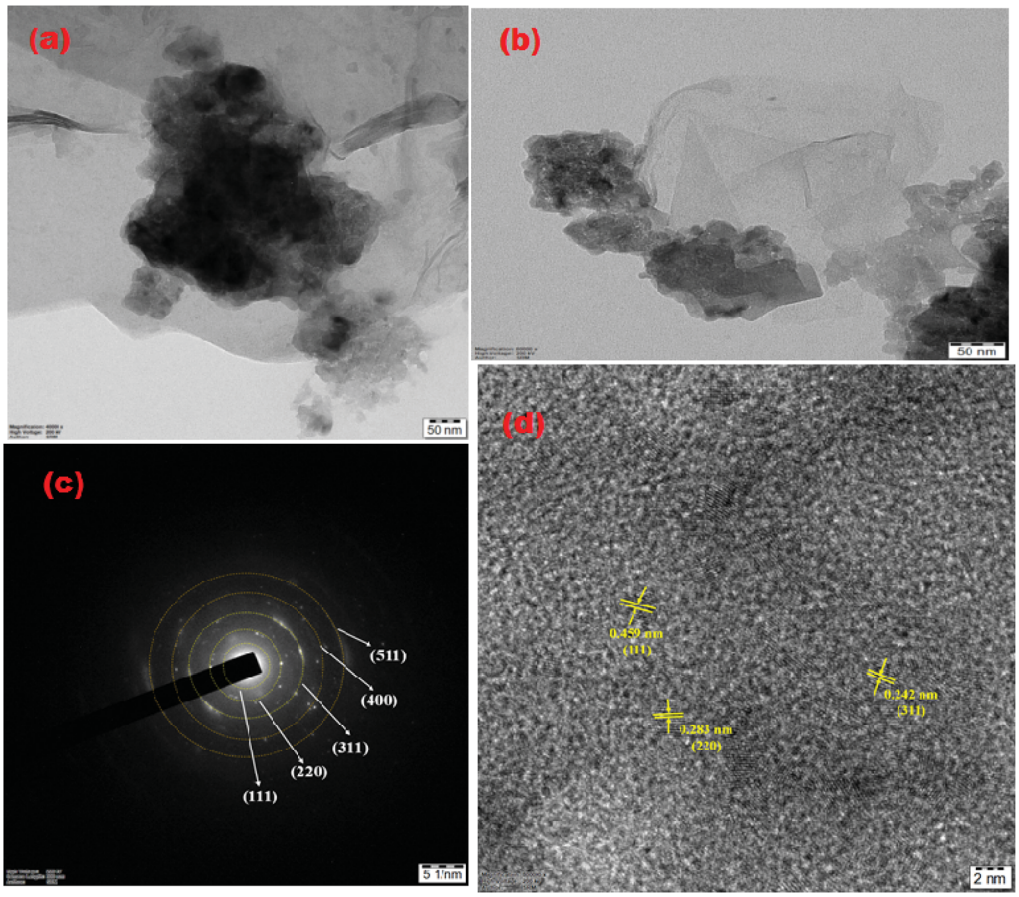

Fig. 4 (a and b) TEM images of the $NiCo_2O_4$/S-rGO composite, (c) SAED pattern of $NiCo_2O_4$/S-rGO and (d) HRTEM result of the $NiCo_2O_4$/S-rGO composite.

decorated both at the edges and basal plane on rGO due to the electrostatic force of attraction between the functional groups of rGO and metal ions. The EDX spectrum of pristine $NiCo_2O_4$ shown in Fig. 3(c) exhibits the peaks of Ni, Co and O atoms alone confirming the purity of the sample. The EDX spectrum of $NiCo_2O_4$/rGO is shown in Fig. 3(f) which further confirmed that $NiCo_2O_4$ bonded well with rGO and no extra peaks were observed confirming that the composite was formed successfully. Fig. 3(i) and (l) show the EDX spectra of $NiCo_2O_4$/S-rGO and $NiCo_2O_4$/S,N-rGO composites, respectively, and it was obvious that sulphur (S) was doped into the carbon network of $NiCo_2O_4$/S-rGO and both S and N were doped into the graphene network anchored by $NiCo_2O_4$ nanostructures.

TEM analysis further revealed the growth of $NiCo_2O_4$ nanoparticles with the diameter ranging from 10 to 20 nm on rGO sheets as displayed in Fig. 4(a) and (b). The SAED pattern of the $NiCo_2O_4$/S-rGO composite (Fig. 4(c)) exhibited multiple diffraction facets indicating that the $NiCo_2O_4$/S-rGO composite was polycrystalline. Fig. 4(d) shows the HRTEM image of the $NiCo_2O_4$/S-rGO nanocomposite which showed interlayer spacings of 0.242 nm, 0.283 nm and 0.459 nm which were attributed to the (311), (220) and (111) planes, respectively, of $NiCo_2O_4$.

To investigate the oxidation state of the elements present in the $NiCo_2O_4$/S-rGO electrocatalyst, XPS measurements were performed. The survey spectrum of the $NiCo_2O_4$/S-rGO sample presented in Fig. 5(a) shows the presence of all the elements, *i.e.*, Ni, Co, S, C and O, confirming the successful formation of the composite. Fig. 5(b) shows the deconvoluted spectrum of Ni 2p in which the low energy band at 856.2 eV corresponded to the Ni $2p_{3/2}$ state and the high energy band at 874.2 eV was attributed to the Ni $2p_{1/2}$ oxidation state. The spectrum also revealed the existence of shakeup satellite peaks (marked as "sat.") at 878.4 eV and 862.1 eV, respectively.[38,39] The *spin–orbit* doublets of the Ni^{2+} oxidation state were observed at binding energies of 854.9 and 871.0 eV, respectively, and those of the Ni^{3+} oxidation state were observed at binding energies of 856.5 eV and

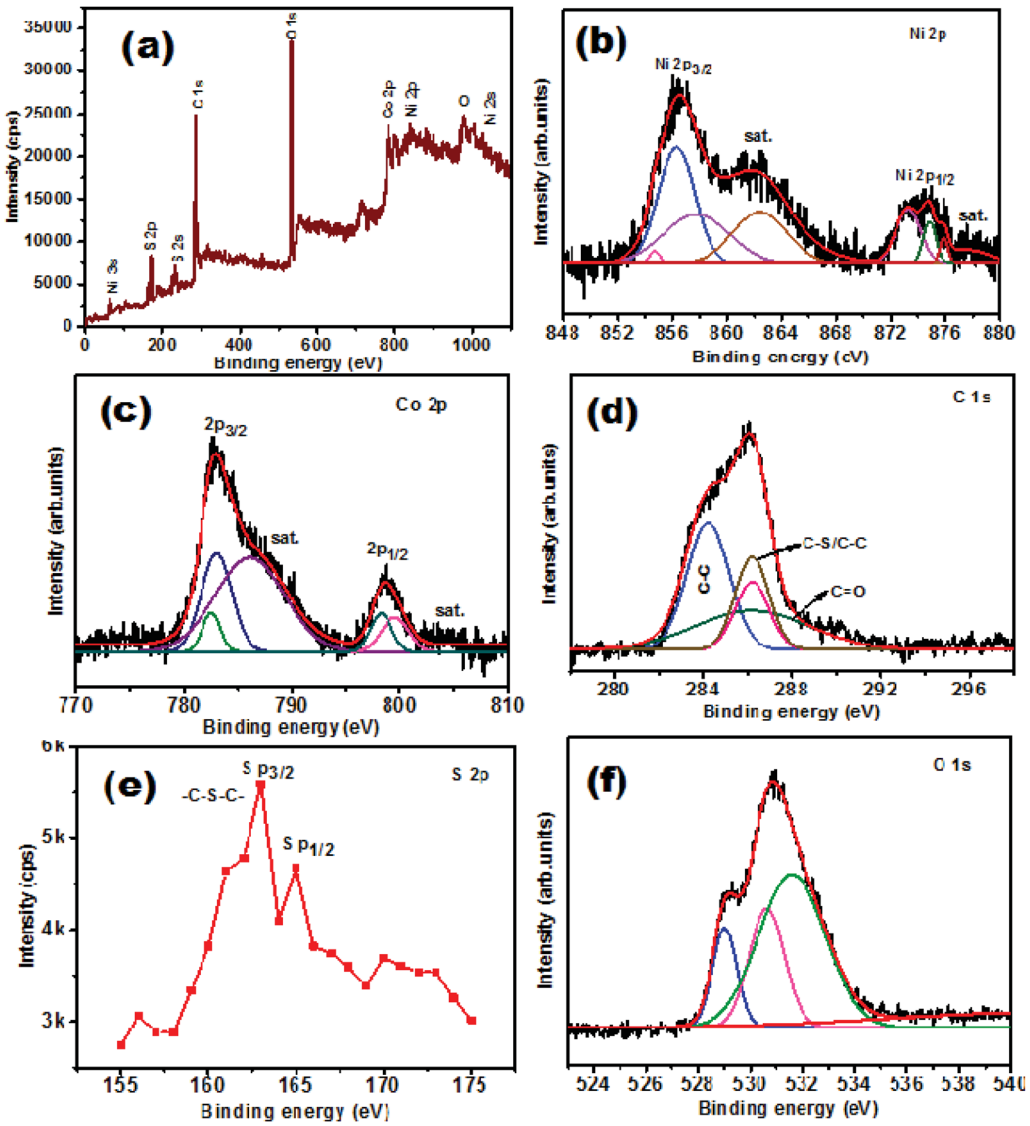

Fig. 5 (a) XPS survey spectrum of $NiCo_2O_4$/S-rGO, and high resolution spectra of (b) Ni 2p, (c) Co 2p, (d) C 1s, (e) S 2p, and (f) O 1s.

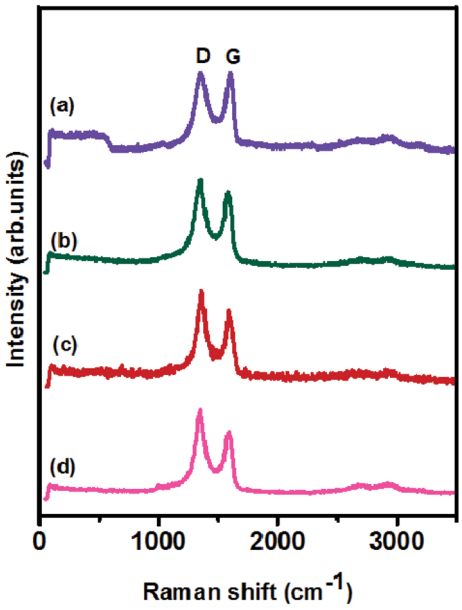

Fig. 6 Raman spectra of (a) GO, (b) $NiCo_2O_4$/rGO, (c) $NiCo_2O_4$/S-rGO and (d) $NiCo_2O_4$/S,N-rGO.

862.3 eV, respectively. The deconvoluted spectrum of Co 2p is shown in Fig. 5(c) and consists of two major peaks observed at 782.2 eV and 798.2 eV. These peaks correspond to Co $2p_{3/2}$ and Co $2p_{1/2}$ oxidation states, respectively, and the peaks observed at 785.4 and 802.6 eV were attributed to satellite peaks (denoted as sat.). Also, the deconvoluted peaks at 782.2 and 797.4 eV were attributed to the Co^{2+} oxidation state and the peaks at binding energies of 780.1 and 795.2 eV confirmed the existence of the Co^{3+} oxidation state.[38,40,41,67] The order of intensity of the Co 2p satellite peak was remarkably higher than that of other spinels which might be due to the increased order of hydroxylation of cobaltites which helps in stimulating OER activity.[39] The C 1s spectrum shown in Fig. 5(d) revealed four fitted peaks at binding energies of 284.2, 285.6, 286 and 286.8 eV, respectively, which were attributed to C–S–C, C–S, C–O–C and C=O bonding, respectively. This strongly indicates that sulphur atoms were successfully doped into the carbon network. The high resolution spectrum of S 2p is displayed in Fig. 5(e) and it is worth noting that the obvious peaks at 163.1 eV and 164.8 eV were ascribed to S $p_{3/2}$ and S $p_{1/2}$ oxidation states, respectively.[42,44] The deconvoluted O 1s spectrum is shown in Fig. 5(f) with the peaks fitted at binding energies of 529.1, 530.5 and 531.5 eV,

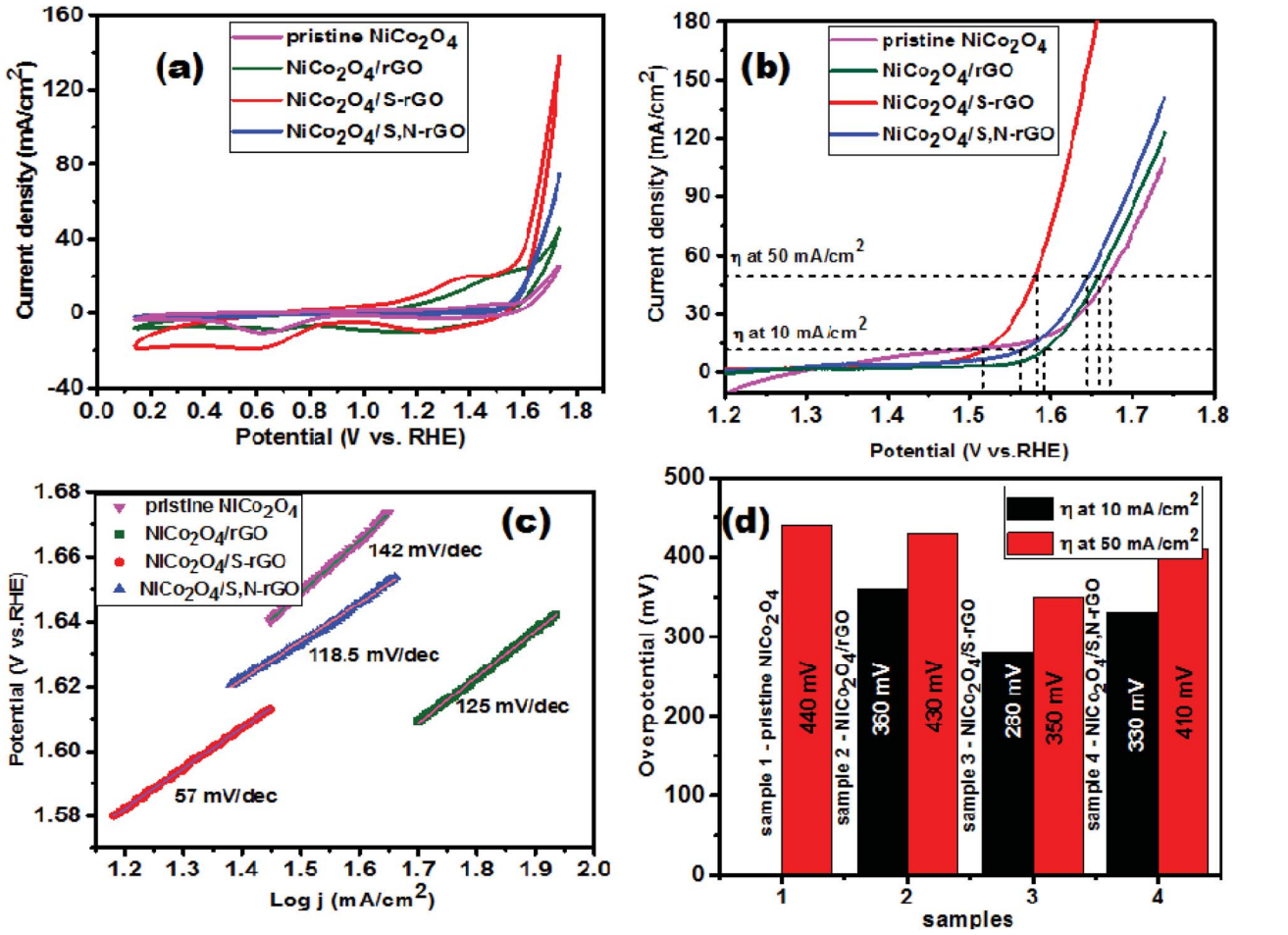

Fig. 7 (a) CV curves recorded in 1 M KOH, (b) LSV curves recorded in 1 M KOH, (c) Tafel plots, and (d) comparison of overpotential (η) required to deliver current densities of 10 and 50 mA cm^{-2}.

respectively. The peaks observed at 529.1 eV and 530.5 eV were attributed to bonding between metal/oxygen and defective sites, respectively. Meanwhile, the peak observed at 531.5 eV was ascribed to the chemisorbed water molecules.[43]

Structural analysis of the prepared catalysts was performed using Raman spectroscopy and the results are displayed in Fig. 6. The Raman spectra of pristine GO and the $NiCo_2O_4$/rGO, $NiCo_2O_4$/S-rGO and $NiCo_2O_4$/S,N-rGO composites are shown in Fig. 6(a)–(d), respectively. All the spectra exhibited a D band centered at 1350 cm^{-1} and a G band at 1590 cm^{-1}. The D band and G band provided information about the degree of distortion in the carbon network due to doping and co-doping of heteroatoms and graphitic sp^2-hybridized carbon, respectively. The ratio between the intensity of the D band (I_D) and G band (I_G) defines the degree of defect levels in the carbon network.[46] Pristine GO has an I_D/I_G ratio of 0.84, while the I_D/I_G ratios of $NiCo_2O_4$/rGO, $NiCo_2O_4$/S-rGO and $NiCo_2O_4$/S,N-rGO composites exhibit higher ratio values of 0.94, 1.04 and 1.122, corroborating that imperfections were introduced by heteroatom doping into the graphene structure.[45]

3.3 Electrocatalysis of the OER

The electrocatalytic performance of the developed electrocatalytic materials was initially investigated using cyclic voltammetry (CV) performed at a sweep rate of 50 mV s^{-1} in the potential range from 0.2 to 1.8 V *vs.* RHE in alkaline medium. Prior to acquiring data, the modified electrodes were subjected to potential cycling for different number of cycles to attain the stable state. The CV curves of pristine $NiCo_2O_4$, and $NiCo_2O_4$/rGO and $NiCo_2O_4$/S-rGO nanocomposites shown in Fig. 7(a) displayed a redox peak in the potential range from 1.2 to 1.45 V *vs.* RHE which was attributed to the conversion of redox couples Co^{2+}/Co^{3+} and Ni^{2+}/Ni^{3+}, respectively.[47] The sharp anodic peak noticed in the $NiCo_2O_4$/S-rGO nanocomposite was ascribed to the transition from the Co^{3+} oxidation state to the Co^{4+} state followed by the evolution of oxygen molecules.[48] This occurred due to the increased electrophilicity arising from a greater number of –OOH intermediates that were generated which in turn decompose and release O_2 molecules more efficiently. This results in enhanced electrocatalytic performance with rapid evolution of oxygen molecules. Moreover, the same catalyst also

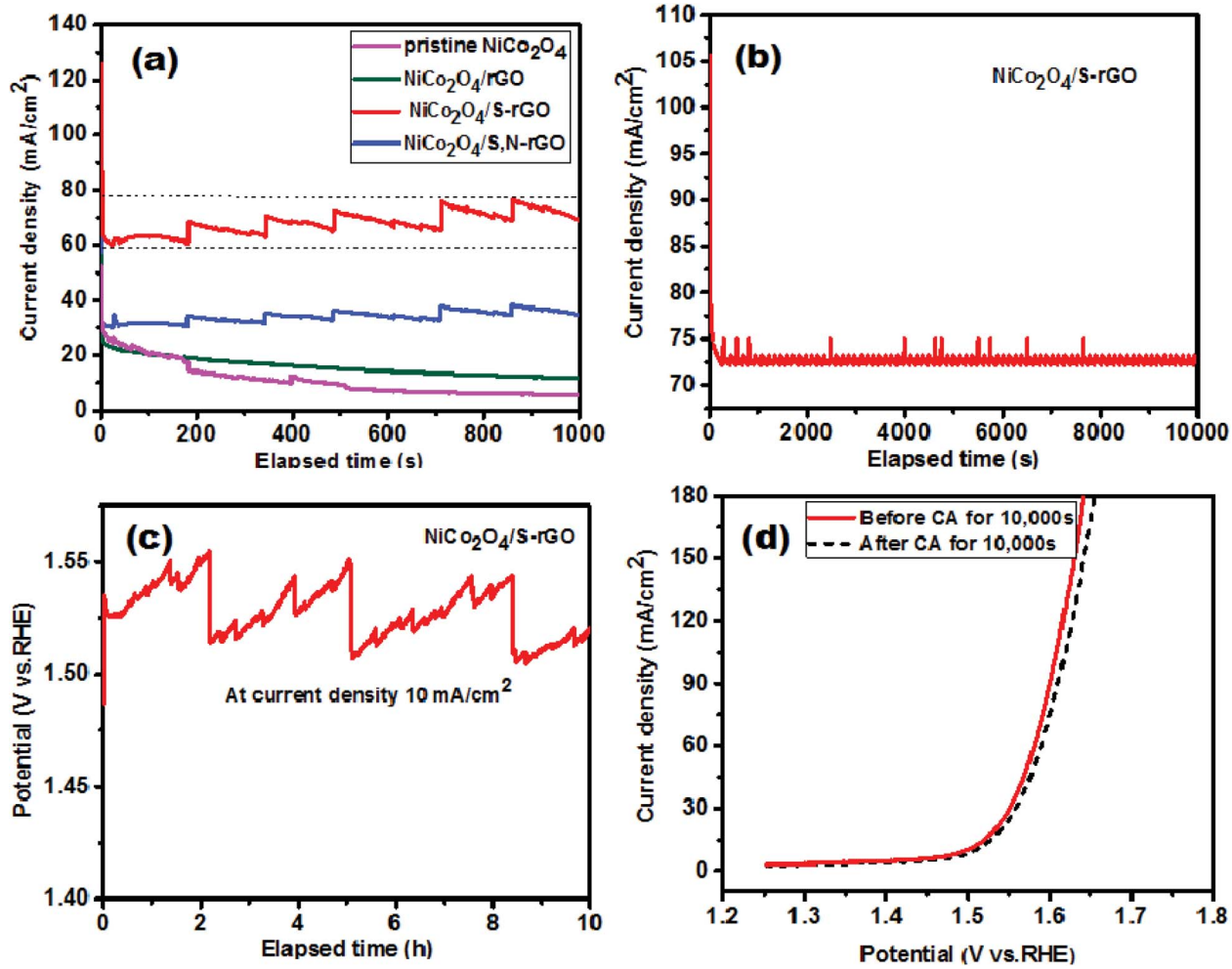

Fig. 8 (a) CA performed at a constant potential of 1.52 V *vs.* RHE for 1000 s, (b) chronoamperometry curve for $NiCo_2O_4$/S-rGO recorded at a potential of 1.52 V *vs.* RHE for 10 000 s, (c) chronopotentiometry conducted for $NiCo_2O_4$/S-rGO at a current density of $J = 10$ mA cm^{-2} for 10 h, and (d) LSV curves recorded for the $NiCo_2O_4$/S-rGO sample before (solid line) and after (dotted line) performing CA for 10 000 s.

delivered a higher current density of 180 mA cm^{-2} when compared with other catalysts which clearly indicates that the $NiCo_2O_4$/S-rGO nanocomposite exhibits superior electrocatalysis towards the OER.

To assess the OER catalytic activity of the prepared samples, linear sweep voltammograms (LSVs) were recorded in 1 M KOH solution after 50 potential sweeps at a scan rate of 5 mV s^{-1}. The polarization curves are displayed in Fig. 7(b) and it was clearly observed that the $NiCo_2O_4$/S-rGO catalyst outperforms the other catalysts with low overpotentials of 280 mV and 350 mV required to deliver current densities of 10 and 50 mA cm^{-2}, respectively. The enhanced electrocatalytic performance was attributed to the electro-oxidation of Ni^{2+} to NiOOH and conversion of the CoOOH oxidation state to CoO_2.[49] In addition, the incorporated sp^2 hybridized carbon substrate possessing more defective sites for electron movement emerged during reduction from GO which also helped in enhancing OER catalysis by adsorbing the intermediate products and releasing O_2 molecules with a lower energy barrier. Moreover, doping with heteroatoms further improved the catalytic efficiency as they were capable of adsorbing the intermediate products formed during oxidation of water. In this context, binding of oxygen and its reactivity with an element is an important parameter to be assessed for catalytic applications. Since S is less electronegative than N, carbon atoms at the adjacent edges become less positively charged in S-doped carbon when compared with those in N-doped carbon. Hence, the assimilation of negatively charged hydroxide ions (OH^-) happens easily and vigorously on N-doped carbon. The adsorption of intermediates in N-doped carbon was much stronger while the dissociation of the final product (O_2) was more strenuous in N-doped carbon when compared with other heteroatom doped carbon.[25] This suggested that the $NiCo_2O_4$/S-rGO electrocatalyst showed enhanced catalytic performance in oxidation of water due to its low oxophilicity properties. Thus it strongly proves that oxophilicity plays a vital role in water oxidation relative to the electrophilicity of the dopants. The catalytic performance was compared with a few spinel $NiCo_2O_4$ based electrocatalysts and is tabulated in Table 2.

To assess the kinetic behaviour of OER catalytic activity, Tafel plots were fitted by re-plotting the polarization curves with log of current density on the x-axis and overpotential on the y-axis and are presented in Fig. 7(c). The slope obtained from the linear fit was considered as the Tafel slope and was described as $d\log(j)/d\eta = 2.303RT/\alpha nF$. From the formula it was observed that the Tafel slope value reveals the number of electrons transferred during the electrocatalytic reaction.[50,51] In this regard, the $NiCo_2O_4$/S-rGO electrocatalyst has a small Tafel slope value of 57 mV dec^{-1} when compared with the other electrocatalysts indicating that the electrocatalyst is more efficient in electron transfer as a consequence of bonding of sp^2 hybridized carbon with $NiCo_2O_4$ nanostructures and heteroatom doping into the graphitic structure. This resulted in superior OER catalytic performance when compared with the other catalysts. Fig. 7(d) shows the comparison plot of the overpotentials required in pristine $NiCo_2O_4$, $NiCo_2O_4$/rGO and $NiCo_2O_4$/S-rGO electrocatalysts to achieve current densities of 10 and 50 mA cm^{-2}.

Stability of the electrocatalyst is an essential parameter to be investigated before its practical use in large scale applications. Hence, it was analyzed using the chronoamperometry technique for the prepared samples. The short-term stability of all the catalysts was evaluated at a stable applied potential of 1.52 V *vs.* RHE for 1000 s and the results are shown in Fig. 8(a). The stability of the $NiCo_2O_4$/S-rGO catalyst is found to be superior to that of the other catalysts when subjected to a continuous electrolysis process for a short time period of 1000 s. Initially, for the $NiCo_2O_4$/S-rGO catalyst the current density was found to be 121.5 mA cm^{-2} and as water oxidation began the current density decreased to 62.4 mA cm^{-2} and remained stable thereafter up to 1000 s. Moreover, the zig-zag pattern noticed in the CA curve was due to evolution of oxygen bubbles while a few bubbles remained on the surface of the electrode and destroyed the electrocatalytic performance. The CA curve for the same catalyst ($NiCo_2O_4$/S-rGO) was recorded for 10 000 s to evaluate its long-term stability and is depicted in Fig. 8(b). It exhibited good stability by sustaining maximum (65%) current density which implies that it can be used in real time application. In the same manner, stability of the $NiCo_2O_4$/S-rGO electrocatalyst was

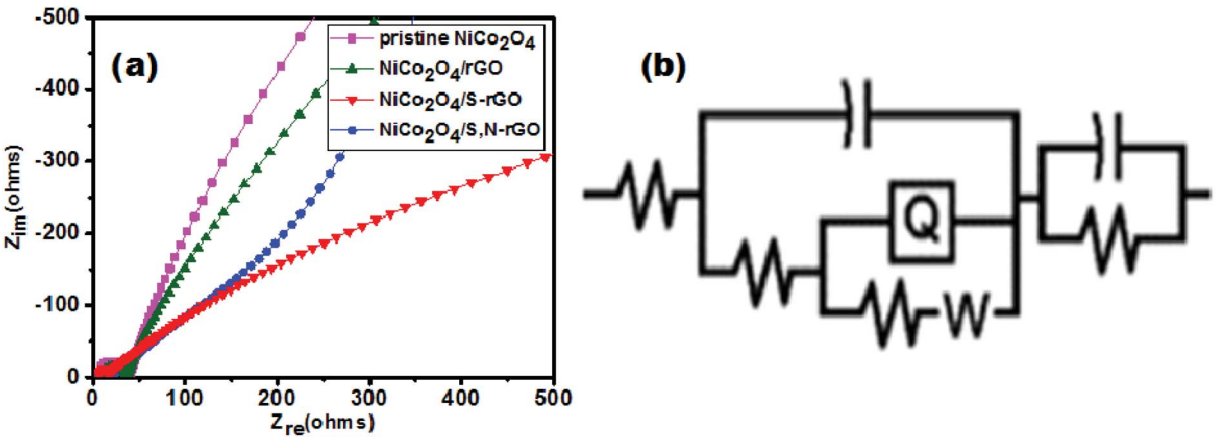

Fig. 9 (a) EIS spectra of all catalysts and (b) equivalent circuit.

further demonstrated *via* chronopotentiometry analysis at an applied current density of 10 mA cm^{-2} for 10 h and the result is displayed in Fig. 8(c). It was observed that there is a negligible increase in potential and a constant response during its catalytic performance measurement for 10 h. These findings further proved that the $NiCo_2O_4$/S-rGO composite can be employed as an electrocatalyst for the OER in large scale application. Fig. 8(d) shows a comparison of polarization curves recorded before and after performing CA for 10 000 s. The result showed slight variation after conducting chronoamperometry analysis for 10 000 s. This strongly proved its efficiency and stability in the evolution of oxygen molecules.

The charge transfer ability of the prepared electrocatalysts was demonstrated using Electrochemical Impedance Spectroscopy (EIS). The Nyquist plots for pristine $NiCo_2O_4$, and $NiCo_2O_4$/rGO, $NiCo_2O_4$/S-rGO and $NiCo_2O_4$/S,N-rGO composites are presented in Fig. 9(a). The plots were recorded in the frequency range of 10 kHz to 0.1 Hz with an applied AC amplitude of 20 mV. The EIS spectra of all the electrocatalysts consisted of a suppressed semicircle in the high frequency region which was attributed to charge transfer resistance (R_{ct}). The suppressed figure of the semicircle is attributed to the presence of a CPE (constant phase element).[52]

The straight line corresponds to Warburg resistance (W_d) which arises from the penetration of ions through the electrolyte solution. The experimentally obtained EIS spectra were fitted with the equivalent circuit as shown in Fig. 9(b). It contains R_s (solution resistance), R_{ct} (charge transfer resistance), CPE, C_{dl} (double layer capacitance) and W_d (Warburg resistance).[47,53] The R_{ct} is of utmost importance as it describes the degree of conductivity and the R_{ct} values are tabulated in Table 1. It was evident from the result that the catalysts bonded with the rGO carbon structure possess a small R_{ct} value when compared with the $NiCo_2O_4$ pristine catalyst owing to its large specific surface area and greater number of active sites. Moreover, heteroatom doping further increased the conductivity of the catalyst by replacing carbon atoms from the appropriate location. Thus it illustrates that the conductivity of the catalyst is maximum with rapid electron transfer which helps in stimulating the OER process.

Determination of the electrochemically active surface area (ECSA) is a key factor as it is an important parameter in stimulating OER activity. Greater the number of active surface sites, higher is the electrocatalytic performance. ECSA is calculated from the fraction of C_{dl} and C_S as shown below

$$\mathrm{ECSA} = C_{dl}/C_S \quad (2)$$

In order to calculate the C_{dl} values, cyclic voltammetry curves were recorded at different scan rates in the non-faradaic potential region of 0.5 to 0.6 V *vs.* Hg/HgO initially which is shown in Fig. 10(a). The recorded CV curves exhibited a rectangular shape which depicted the characteristics of electric double layer capacitance (EDLC). In addition, there occurred no charge transfer in the non-faradaic region, while the current was generated from the electric double layer (EDL). The specific capacitance (C_s) of the catalyst coated surface was considered to be 60 μF cm^{-2} which was reported in earlier studies.[50,54]

A linear fit was obtained by plotting the scan rate against current density measured at a potential of 0.55 V *vs.* Hg/HgO and is shown in Fig. 10(b). The slope value of the linear plot (*i.e.*, $i = C(dE/dt)$) corresponds to the C_{dl} value.[24] The roughness factor (R_f) also plays a significant role in enhancing the catalytic performance and was calculated from the ratio of ECSA and geometric surface area (0.0732 cm^2) of the electrode.[51] The calculated values of ECSA and R_f are tabulated in Table 1. The $NiCo_2O_4$/S-rGO electrocatalyst exhibits a greater ECSA value suggesting that the catalyst contains a large number of active sites due to heteroatom doping into the graphitic structure which altered the energy bands resulting in creation of valences. Also, due to reduction of GO more active sites have been generated by partial removal of functional groups which is also beneficial for improving the OER performance.

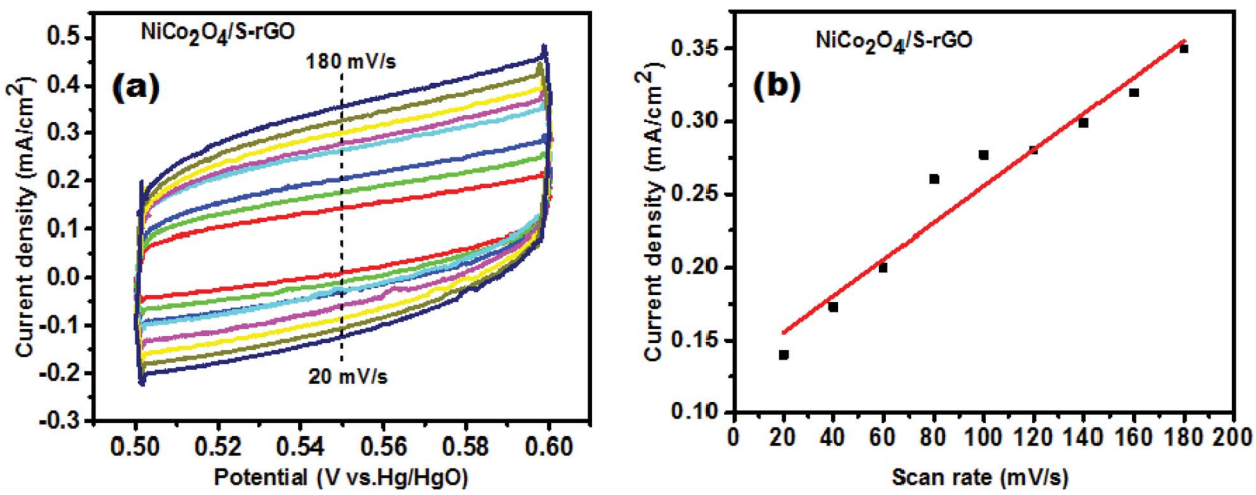

Fig. 10 (a) CV curves measured in the potential range of 0.5 to 0.6 V *vs.* Hg/HgO for the $NiCo_2O_4$/S-rGO catalyst, and (b) linear fit of current density *vs.* scan rate.

Faradaic efficiency is an important parameter to evaluate the efficiency of the catalyst. The faradaic efficiency of the catalyst modified electrode was calculated using the collection efficiency for which the $NiCo_2O_4$/S-rGO catalyst was drop-cast on a glassy carbon (GC) disk and allowed to dry at ambient temperature without disturbing the Pt ring. A linear sweep voltammogram (Fig. S1†) was acquired at a sweep rate of 5 mV s^{-1} at 1600 rpm by sweeping the potential at the disk from 1.1 to 1.75 V *vs.* RHE and the evolved O_2 molecules were reduced at the Pt ring. The faradaic efficiency was calculated using the following equation.

$$\text{Faradaic efficiency} = I_R \times n_D / I_D \times n_R \times N_{CL} \quad (3)$$

where I_R corresponds to the ring current due to oxygen reduction at the Pt ring, I_D is the disk current arising from oxygen evolution at the GC disk electrode, n_D and n_R describe the number of electrons transferred during O_2 evolution and reduction and the parameter N_{CL} indicates the collection efficiency of the RRD electrode, which is found to be 0.3684 and was calculated following a procedure reported earlier.[48] The calculated faradaic efficiency at 1.56 V is 98.23%. This clearly reveals that O_2 evolution is more dominant than the electrochemical oxidation of Ni^{2+} to Ni^{3+} at 1.56 V *vs.* RHE. The loss of 1.77% might be due to the ohmic drop associated with the diffusion of O_2 evolved, and the voltammetric response observed at the disk electrode does not depend on rotation rate which implies that electrocatalytic oxidation of water molecules is kinetically limited.

The turnover frequency is also an important factor of interest which gave an insight into intrinsic OER electrocatalysis.[1,66] It was calculated by considering 100% activity of all the atoms participating in the catalytic reaction.[53] The TOF value was calculated for the $NiCo_2O_4$/S-rGO catalyst, which delivered an overpotential (η) of 280 mV, using the equation (eqn (4)) presented below

$$\text{TOF} = J_{geo}/4 \times F \times n \quad (4)$$

where J_{geo} represents the current density at the corresponding overpotential value (280 mV) of $NiCo_2O_4$/S-rGO, F is the Faraday constant (96 485.4 C mol^{-1}) and n corresponds to the number of moles. The TOF value of the $NiCo_2O_4$/S-rGO catalyst was found to be 5.14×10^{-4} s^{-1}. The TOF values of other catalysts are tabulated in Table 1. The greater TOF value is due to the combined synergetic effect of metal atoms coupled with heteroatom (S) doped rGO providing electrochemically accessible sites.

Table 2 Comparison of few $NiCo_2O_4$ spinel based electrocatalysts

Catalyst	$\eta_{j=10\ mA\ cm^{-2}}$ (mV)	Tafel slope (mV dec^{-1})	Electrolyte	References
$NiCo_2O_4$ hollow microcuboids	420	53.0	1 M NaOH	7
$NiCo_2O_4$ microflowers	350	54	0.1 M KOH	12
$NiCo_2S_4$ on nickel foam	279	68	1 M KOH	13
$NiCo_2O_4$ rosette-like hierarchical spinel	670	89	1 M KOH	15
$NiCo_2O_4$ 3-D nanoflowers	383	137	1 M KOH	21
Chrysanthemum flower-like $NiCo_2O_4$–nitrogen doped graphene oxide	400	—	0.1 M KOH	28
$NiCo_2O_4$ ultrathin nanosheets	340	75	0.1 M KOH	29
$NiCo_2O_4$-rGO	381	45.7	1 M KOH	32
$NiCo_2O_4$ nanoframes with a nanosheet surface	265	82	1 M KOH	39
$NiCo_2S_4$ spheres grown on N,S co-doped rGO	340	65	0.1 M KOH	45
Zinc-doped $NiCo_2O_4$	420	62.0	0.1 M KOH	55
$NiCo_2O_4$ *via* KIT-6	350	43.0	1 M KOH	56
Hierarchical hollow urchin-like $NiCo_2O_4$	419	43.9	1 M NaOH	57
$NiCo_2O_4$/NiO/CoF_2@mC_{700} composite	330	70.0	0.1 M KOH	58
Nitrogen-doped graphene-$NiCo_2O_4$	373 at 5 mA cm^{-2}	156.0	0.1 M KOH	59
Co_3O_4/$NiCo_2O_4$ double-shelled nanocages	340	88.0	1 M KOH	60
$NiCo_2O_4$/NiO	360	61	1 M NaOH	61
$NiCo_2O_4$/VN nanoparticles	385	69.4	1 M KOH	62
$NiCo_2O_4$@NiWS nanosheets	290	95.2	1 M KOH	63
$NiCo_2O_4$/S-rGO	**280**	**57**	**1 M KOH**	**This work**

3.4 Electrocatalysis of the MOR

The electrocatalytic activity towards the MOR using the fabricated samples (pristine $NiCo_2O_4$, $NiCo_2O_4$/rGO, $NiCo_2O_4$/S-rGO and $NiCo_2O_4$/S,N-rGO) was evaluated by cyclic voltammetry in 1 M KOH solution before and after addition of methanol. Before recording CV curves, the prepared electrodes were subjected to potential cycling for 30 cycles to attain the stable state. Fig. 11(a–d) show the relative CV curves of the pristine $NiCo_2O_4$, $NiCo_2O_4$/rGO, $NiCo_2O_4$/S-rGO and $NiCo_2O_4$/S,N-rGO electrocatalysts recorded with and without addition of methanol in the

Table 1 Onset potential, Tafel slope, overpotential measured at 10 mA cm^{-2}, and calculated values of ECSA, R_f, and R_{ct} from EIS

Catalyst	Onset potential (V *vs.* RHE)	Tafel slope (mV dec^{-1})	Overpotential η (mV) at 10 mA cm^{-2}	ECSA (cm^2)	R_f	R_{ct} (Ω)	TOF × 10^{-4} (s^{-1})
Pristine $NiCo_2O_4$	1.58	142	—	0.54	7.37	47.3	—
$NiCo_2O_4$/rGO	1.55	125	360	0.98	13.38	28.2	4.53
$NiCo_2O_4$/S-rGO	1.48	57	280	2.23	30.46	8.23	5.14
$NiCo_2O_4$/S,N-rGO	1.52	118.5	320	1.08	14.7	10.8	5.41

potential range from 0.8 to −0.8 V *vs.* Hg/HgO at a scan rate of 50 mV s^{-1}. It is worth noting that all the CV curves exhibit redox peaks in the anodic and cathodic sweeps corroborating the transfer of oxidation states (Ni^{2+}/Ni^{3+} and Co^{2+}/Co^{3+}) of Ni and Co atoms. In addition, the anodic current density increased sharply after addition of 0.5 M methanol, undoubtedly revealing the outstanding electrochemical activity of all electrocatalysts towards the oxidation of methanol. The current densities of pristine $NiCo_2O_4$, $NiCo_2O_4$/rGO, $NiCo_2O_4$/S-rGO and $NiCo_2O_4$/S,N-rGO were found to be 78.6, 138.5, 140.8 and 203. 4 mA cm^{-2}, respectively. Among all the electrocatalysts, $NiCo_2O_4$/S,N-rGO exhibits superior electrocatalytic MOR as depicted in Fig. 11(d), with an elevated current density of 203.4 mA cm^{-2} and extremely low onset potential of 0.12 V *vs.* Hg/HgO when compared with other catalysts. This is mainly accredited to the existence of a greater number of active accessible electrocatalytic sites compared to other catalysts which leads to better electrocatalytic activity.

The oxidative species of Ni and Co atoms *i.e.*, hydroxides and oxy-hydroxides formed during electrochemical reaction afford rich active sites for stimulating catalytic oxidation of methanol.[64] Moreover, $NiCo_2O_4$ nanostructures coupled with rGO and heteroatom (S & N) co-doping into the carbon network of rGO also significantly improve the catalytic performance by enhancing the electron transfer easily.[35] The coupled rGO helps in chemisorption of CO molecules and dissociation of other intermediate products formed during oxidation of methanol.[65] Also, because of the doped heteroatoms, owing to the variation in electronegativity and size when compared with carbon, there occurs structural distortion and difference in charge density in the carbon network. This generates a greater number of topological defects in the graphene sheet, which therefore enhances the electron transport and thereby improves the electrochemical activity with the attainment of higher current density. They also serve as adsorption sites for adsorbing intermediate products formed during electro-oxidation of methanol.

The stability of the outperforming catalyst ($NiCo_2O_4$/S,N-rGO) was investigated using the CA technique at a persistent potential of 0.4 V *vs.* Hg/HgO for a duration of 1000 s and is displayed in Fig. 12(a). The catalyst revealed excellent stability by sustaining a maximum order of current density showing that it can serve as a better electrocatalyst for oxidation of methanol.

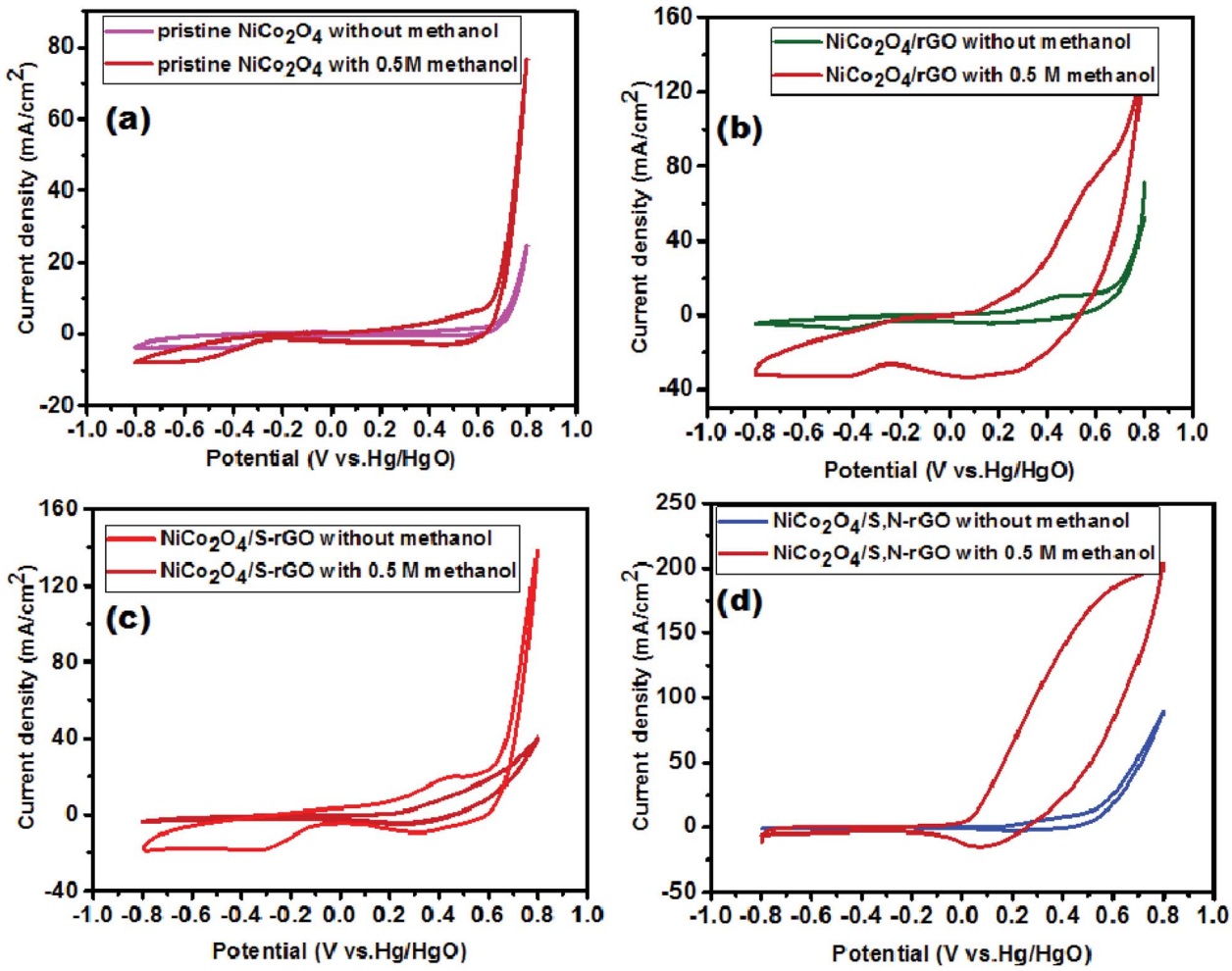

Fig. 11 CV curves recorded in 1 M KOH solution before and after addition of methanol for (a) pristine $NiCo_2O_4$, (b) $NiCo_2O_4$/rGO, (c) $NiCo_2O_4$/S-rGO and (d) $NiCo_2O_4$/S,N-rGO.

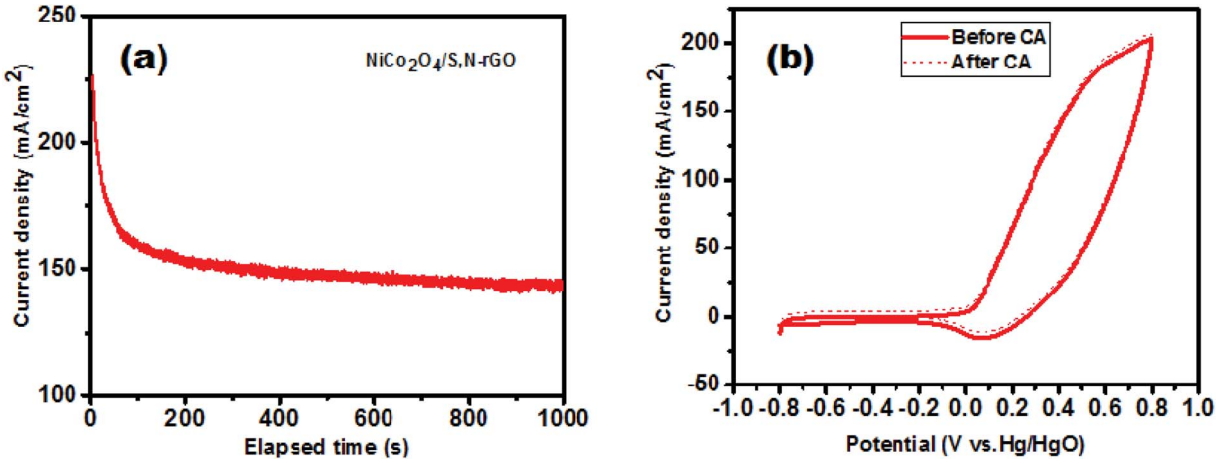

Fig. 12 (a) CA curve measured at a constant potential of 0.4 V *vs.* Hg/HgO for 1000 s and (b) CV curve recorded before (solid line) and after CA (dotted line).

The stability of the catalyst was also further proven by recording its CV curve after performing CA for 1000 s which is shown in Fig. 12(b). Hence, the $NiCo_2O_4$/S,N-rGO electrocatalyst can be employed as an anode catalyst in DMFCs for practical applications.

3.5 Mechanism of the MOR

The methanol oxidation reaction is a complex multi-step process. It proceeds as a slower reaction and the reaction proceeds through multiple steps. The possible routes to the complete oxidation of methanol are as follows. Initially, the methanol which is fed to the anode part is oxidized to formaldehyde, which is then oxidized to formic acid. Finally, formic acid is oxidized to carbon dioxide. In some cases, the fed methanol may take another route, which forms carbon monoxide as an intermediate product. The carbon monoxide acts as a poison to the generally used platinum catalyst at the anode of the DMFC.

4 Conclusion

A set of electrocatalysts (pristine $NiCo_2O_4$, $NiCo_2O_4$/rGO, $NiCo_2O_4$/S-rGO and $NiCo_2O_4$/S,N-rGO) were developed by a simple hydrothermal technique and their electrocatalytic performance towards oxygen evolution was investigated. To enhance the electron conductivity and catalytic efficiency, spinel $NiCo_2O_4$ was coupled with rGO. To further improve the efficacy of the electrochemical reaction heteroatoms were doped and co-doped into the graphitic network, which alters the electronic band structure and helps in improving oxidation of water molecules. As a result, $NiCo_2O_4$/S-rGO outperformed the other catalysts due to its low oxophilicity and good conducting nature when compared with the other catalysts. The catalyst required an overpotential of 280 mV to deliver a current density of 10 mA cm^{-2} and exhibited a small Tafel slope of 57 mV dec^{-1}. The same set of electrocatalysts were also investigated towards oxidation of methanol in which the $NiCo_2O_4$/S,N-rGO catalyst showed outstanding performance with an extremely low onset potential (0.12 V) and high current density (203.4 mA cm^{-2}). This was accredited to the combined effect of existence of multiple oxidation states of Ni and Co atoms and co-doped heteroatoms which causes defects in the obtained rGO sheets.

Conflicts of interest

There are no conflicts to declare.

Acknowledgements

The authors thank the funding agencies DST-SERB (EMR/2016/007676), UGC-SAP, DST-FIST and DST-PURSE, Government of India for providing the required instrumentation facilities for our Department.

References

1 S. Anantharaj, S. Rao Ede, K. Sakthikumar, K. Karthick, S. Mishra and S. Kundu, Recent Trends and Perspectives in Electrochemical Water Splitting with an Emphasis on Sulfide, Selenide, and Phosphide Catalysts of Fe, Co, and Ni: A Review, *ACS Catal.*, 2016, **6**, 8069–8097.

2 J.-J. Duan, R. L. Zhang, J.-J. Feng, L. Zhang, Q.-L. Zhang and A.-J. Wang, Facile synthesis of nanoflower-like phosphorus-doped $Ni_3S_2/CoFe_2O_4$ arrays on nickel foam as a superior electrocatalyst for efficient oxygen evolution reaction, *J. Colloid Interface Sci.*, 2021, **581**, 774–782.

3 C. Hu, Z. Yi, W. She, J. Wang, J. Xiao and S. Wang, Urchin-like non-precious-metal bifunctional oxygen electrocatalysts: Boosting the catalytic activity via the In-situ growth of heteroatom (N, S)-doped carbon nanotube on mesoporous cobalt sulfide/carbon spheres, *J. Colloid Interface Sci.*, 2018, **524**, 465–474.

4 M. Li, A. R. Insani, L. Zhuang, Z. Wang, A. ur Rehman, L. X. Liu and Z. Zhu, Strontium-doped lanthanum iron nickelate oxide as highly efficient electrocatalysts for

oxygen evolution reaction, *J. Colloid Interface Sci.*, 2019, **553**, 813–819.

5 X. Xiong, C. You, Z. Liu, A. M. Asiri and X. Sun, Co-Doped CuO Nanoarray: An Efficient Oxygen Evolution Reaction Electrocatalyst with Enhanced Activity, *ACS Sustainable Chem. Eng.*, 2018, **6**, 2883–2887.

6 R. L. Zhang, J.-J. Duan, J.-J. Feng, L. P. Mei, Q. L. Zhang and A. J. Wang, Walnut kernel-like iron-cobalt-nickel sulfide nanosheets directly grown on nickel foam: a binder-free electrocatalyst for high-efficiency oxygen evolution reaction, *J. Colloid Interface Sci.*, 2021, **587**, 141–149.

7 X. Gao, H. Zhang, Q. Li, X. Yu, Z. Hong, X. Zhang, C. Liang and L. Zhan, Hierarchical $NiCo_2O_4$ Hollow Microcuboids as Bifunctional Electrocatalysts for Overall Water-Splitting, *Angew. Chem., Int. Ed.*, 2016, **55**, 6290–6294.

8 A. B. Yousaf, M. Imran, N. Uwitonze, A. Zeb, S. J. Zaidi, T. M. Ansari, G. Yasmeen and S. Manzoor, Enhanced Electrocatalytic Performance of Pt_3Pd_1 Alloys Supported on CeO_2/C for Methanol Oxidation and Oxygen Reduction Reactions, *J. Phys. Chem. C*, 2017, **121**, 2069–2079.

9 X. Yue, C. He, C. Zhong, Y. Chen, S. P. Jiang and P. K. Shen, Fluorine-Doped and Partially Oxidized Tantalum Carbides as Nonprecious Metal Electrocatalysts for Methanol Oxidation Reaction in Acidic Media, *Adv. Mater.*, 2016, **28**, 2163–2169.

10 A. Roy, H. S. Jadhav, M. Cho and G. Jeong Seo, Electrochemical deposition of self-supported in bifunctional copper oxide electrocatalyst for methanol oxidation and oxygen evolution reaction, *J. Ind. Eng. Chem.*, 2019, **76**, 515–523.

11 Y. P. Wu, J.-W. Tian, S. Liu, B. Li, J. Zhao, L. F. Ma, D.-S. Li, Y. Lan and X. Bu, Bi-Microporous Metal-Organic Frameworks with Cubane $[M_4(OH)_4]$ (M = Ni, Co) Clusters and Pore Space Partition for Electrocatalytic Methanol Oxidation Reaction, *Angew. Chem.*, 2019, **131**, 12313–12317.

12 E. Umeshbabu, P. Hari Krishna Charan, P. Justin and G. Ranga Rao, Hierarchically Organized $NiCo_2O_4$ Microflowers Anchored on Multiwalled Carbon Nanotubes: Efficient Bifunctional Electrocatalysts for Oxygen and Hydrogen Evolution Reactions, *ChemPlusChem*, 2020, **85**, 183–194.

13 Y. Gong, J. Wang, Y. Lin, Z. Yang, H. Pan and Z. Xu, Synthesis of 1D to 3D nanostructured $NiCo_2S_4$ on nickel foam and their application in oxygen evolution reaction, *Appl. Surf. Sci.*, 2019, **476**, 600–607.

14 T. Zhang, Z. Li, L. Wang, Z. Zhang and S. Wang, Spinel $CoFe_2O_4$ supported by three dimensional graphene as high-performance bi-functional electrocatalysts for oxygen reduction and evolution reaction, *Int. J. Hydrogen Energy*, 2019, **44**, 1610–1619.

15 J. Béjar, L. Álvarez-Contreras, J. Ledesma-García, N. Arjona and L. G. Arriaga, Electrocatalytic evaluation of Co_3O_4 and $NiCo_2O_4$ rosettes-like hierarchical spinel as bifunctional materials for oxygen evolution (OER) and reduction (ORR) reactions in alkaline media, *J. Electroanal. Chem.*, 2019, **847**, 113190.

16 H. Xu, P. Song, C. Liu, Y. Zhang and Y. Du, Facile construction of ultrafine nickel-zinc oxyphosphide nanosheets as high-performance electrocatalysts for oxygen evolution reaction, *J. Colloid Interface Sci.*, 2018, **530**, 58–66.

17 T. Y. Wei, C.-H. Chen, H.-C. Chien, S.-Y. Lu and C.-C. Hu, A Cost-Effective Supercapacitor Material of Ultrahigh Specific Capacitances: Spinel Nickel Cobaltite Aerogels from an Epoxide-Driven Sol–Gel Process, *Adv. Mater.*, 2010, **22**, 347–351.

18 C. Zhou, J. Mu, Y.-F. Qi, Q. Wang, X.-J. Zhao and E.-C. Yang, Iron-substituted Co-Ni phosphides immobilized on Ni foam as efficient self-supported 3D hierarchical electrocatalysts for oxygen evolution reaction, *Int. J. Hydrogen Energy*, 2019, **44**, 8156–8165.

19 H. Tan, J. Tang, J. Henzie, Y. Li, X. Xu, T. Chen, Z. Wang, J. Wang, I. Yusuke, Y. Bando and Y. Yamauchi, Assembly of Hollow Carbon Nanospheres on Graphene Nanosheets and Creation of Iron–Nitrogen-Doped Porous Carbon for Oxygen Reduction, *ACS Nano*, 2018, **12**, 5674.

20 W. Xia, J. Tang, J. Li, S. Zhang, K. C.-W. Wu, J. He and Y. Yamauchi, Defect-Rich Graphene Nanomesh Produced by Thermal Exfoliation of Metal–Organic Frameworks for the Oxygen Reduction Reaction, *Angew. Chem., Int. Ed.*, 2019, **58**, 1–7.

21 Z. Li, B. Li, J. Chen, P. Qi and P. Shen, Spinel $NiCo_2O_4$ 3-D nanoflowers supported on graphene nanosheets as efficient electrocatalyst for oxygen evolution reaction, *Int. J. Hydrogen Energy*, 2019, **44**(31), 16120–16131.

22 T. Zhang, Z. Li, L. Wang, Z. Zhang and S. Wang, Spinel $CoFe_2O_4$ supported by three dimensional graphene as high-performance bi-functional electrocatalysts for oxygen reduction and evolution reaction, *Int. J. Hydrogen Energy*, 2019, **44**, 1610–1619.

23 J. Yang, M. Xu, J. Wang, S. Jin and B. Tan, A Facile Approach to Prepare Multiple Heteroatom-Doped Carbon Materials from Imine-Linked Porous Organic Polymers, *Sci. Rep.*, 2018, **8**, 4200.

24 T. Asefa and X. Huang, Heteroatom-Doped Carbon Materials for Electrocatalysis, *Chem.–Eur. J.*, 2017, **23**, 10703–10713.

25 F. Razmjooei, K. P. Singh, D.-S. Yang, W. Cui, Y. H. Jang and J.-S. Yu, Fe-Treated Heteroatom (S/N/B/P)-Doped Graphene Electrocatalysts for Water Oxidation, *ACS Catal.*, 2017, **7**, 2381–2391.

26 Y. Zhang, P. Wang, J. Yang, S. Lu, K. Li, G. Liu, Y. Duan and J. Qiu, Decorating ZIF-67-derived cobalt–nitrogen doped carbon nanocapsules on 3D carbon frameworks for efficient oxygen reduction and oxygen evolution, *Carbon*, 2021, **177**, 344–356.

27 Y. Zhang, P. Wang, J. Yang, K. Li, X. Long, L. Meng, K. Zhang and J. Qiu, Fabrication of core-shell nanohybrid derived from iron-based metal-organic framework grappled on nitrogen-doped graphene for oxygen reduction reaction, *Chem. Eng. J.*, 2020, **401**, 126001.

28 P. Moni, S. Hyun, A. Vignesh and S. Shanmugam, Chrysanthemum flower-like $NiCo_2O_4$–nitrogen doped graphene oxide composite: an efficient electrocatalyst for lithium–oxygen and zinc–air batteries, *Chem. Commun.*, 2017, **53**, 7836–7839.

29 W. Liu, J. B. L. Xu, M. Guan, Z. Wang, J. Qiu, Y. Huang, J. Xia, Y. Lei and H. Li, $NiCo_2O_4$ ultrathin nanosheets with oxygen vacancies as bifunctional electrocatalysts for Zn-air battery, *Appl. Surf. Sci.*, 2019, **478**, 552–559.

30 Z.-Q. Liu, Q. Z. Xu, J.-Y. Wang, N. Li, S.-H. Guo, Y.-Z. Su, H.-J. Wang, J.-H. Zhang and S. Chen, Facile hydrothermal synthesis of urchin-like $NiCo_2O_4$ spheres as efficient electrocatalysts for oxygen reduction reaction, *Int. J. Hydrogen Energy*, 2013, **38**, 6657–6662.

31 J. Xu, F. Liu, X. Peng, L. Jing, Y. Yang, D. Jin, H. Jin, X. Wang and B. Hong, Hydrothermal Synthesis of $NiCo_2O_4$/Activated Carbon Composites for Supercapacitor with Enhanced Cycle Performance, *ChemistrySelect*, 2017, **2**, 5189–5195.

32 A. Rebekah, G. Bharath, M. Naushad, C. Viswanathan and N. Ponpandian, Magnetic graphene/chitosan nanocomposite: a promising nanoadsorbent for the removal of 2-naphthol from aqueous solution and their kinetic studies, *Int. J. Biol. Macromol.*, 2020, **159**, 530–538.

33 D. Navadeepthy, A. Rebekah, C. Viswanathan and N. Ponpandian, N-doped Graphene/$ZnFe_2O_4$: a novel nanocomposite for intrinsic peroxidase based sensing of H_2O_2, *Mater. Res. Bull.*, 2017, **95**, 1–8.

34 H. Jiang, Y. Kang, P. Ye, Q. Huang, L. Wang and S. Li, Optimized $NiCo_2O_4$/rGO hybrid nanostructures on carbon fiber as an electrode for asymmetric supercapacitors, *RSC Adv.*, 2018, **8**, 37550.

35 E. Umeshbabu, G. Rajeshkhanna, P. Justin and G. Ranga Rao, Synthesis of mesoporous $NiCo_2O_4$-rGO by solvothermal method for charge storage applications, *RSC Adv.*, 2015, **5**, 66657–66666.

36 A. K. Das, R. K. Layek, N. H. Kim, D. Jung and J. H. Lee, Reduced graphene oxide (RGO)-supported $NiCo_2O_4$ nanoparticles: an electrocatalyst for methanol oxidation, *Nanoscale*, 2014, **6**, 10657–10665.

37 H. Zhang, H. Li, H. Wang, K. He, S. Wang, Y. Tang and J. Chen, $NiCo_2O_4$/N-doped graphene as an advanced electrocatalyst for oxygen reduction reaction, *J. Power Sources*, 2015, **280**, 640–648.

38 Y. Wen, S. Peng, Z. Wang, H. Jiaxin, T. Qin, S. Lu, J. Zhang, D. He, X. Fan and G. Cao, Facile synthesis of ultrathin $NiCo_2S_4$ nano-petals inspired by blooming buds for high-performance supercapacitors, *J. Mater. Chem. A*, 2017, **5**, 7144.

39 Z. Chen, B. Zhao, Y.-C. He, H.-R. Wen, X.-Z. Fu, R. Sun and C.-P. Wong, $NiCo_2O_4$ nanoframes with nanosheet surface as efficient electrocatalysts for oxygen evolution reaction, *Mater. Chem. Front.*, 2018, **2**, 1155–1164.

40 S. Natarajan, S. Anantharaj, R. J. Tayade, H. C. Bajaj and S. Kundu, Recovered Spinel $MnCo_2O_4$ from Spent Lithium Ion Batteries for Enhanced Electrocatalytic Oxygen Evolution in Alkaline Medium, *Dalton Trans.*, 2017, **46**, 14382–14392.

41 M. Cheng, H. Fan, Y. Song, Y. Cui and R. Wang, Interconnected hierarchical $NiCo_2O_4$ microspheres as high-performance electrode materials for supercapacitors, *Dalton Trans.*, 2017, **46**, 9201.

42 Y. Zhang, P. Li, X. Yin, Y. Yan, K. Zhan, J. Yang and B. Zhao, Cobalt sulfide supported on nitrogen and sulfur dual-doped reduced graphene oxide for highly active oxygen reduction reaction, *RSC Adv.*, 2017, **7**, 50246.

43 N. Ullah, W. Zhao, X. Lu, C. J. Oluigbo, S. A. Shah, M. Zhang, J. Xie and Y. Xu, In situ growth of M-MO (M $\frac{1}{4}$ Ni, Co) in 3D graphene as a competent bifunctional electrocatalyst for OER and HER, *Electrochim. Acta*, 2019, **298**, 163–171.

44 S. Bag, B. Mondal, A. K. Das and C. Retna Raj, Nitrogen and Sulfur Dual-Doped Reduced Graphene Oxide: Synergistic Effect of Dopants Towards Oxygen Reduction Reaction, *Electrochim. Acta*, 2015, **163**, 16–23.

45 X. Feng, Q. Jiao, Q. Li, Q. Shi, D. Zheng, Y. Zhao, H. Li, C. Feng, W. Zhou and T. Feng, $NiCo_2S_4$ Spheres Grown on N,S co-doped rGO with High Sulfur Vacancies as Superior Oxygen Bifunctional Electrocatalysts, *Electrochim. Acta*, 2019, 135356.

46 B. P. Vinayan, Z. Zhao-Karger, T. Diemant, V. S. K. Chakravadhanula, N. I. Schwarzburger, M. Ali Cambaz, R. J. Behm, C. Kübel and M. Fichtner, Performance study of magnesium–sulfur battery using a graphene based sulfur composite cathode electrode and a non-nucleophilic Mg electrolyte, *Nanoscale*, 2015, **8**, 3296–3306.

47 B. Sidhureddy, S. Prins, J. Wen, A. Thiruppathi Raj, M. Govindhan and A. Chen, Synthesis and Electrochemical Study of Mesoporous Nickel-Cobalt Oxides for Efficient Oxygen Reduction, *ACS Appl. Mater. Interfaces*, 2019, **20**, 18295–18304.

48 T. Naresh Kumar, S. Sivabalan, N. Chandrasekaran and K. L. Phani, Synergism between polyurethane and polydopamine in the synthesis of Ni–Fe alloy monoliths, *Chem. Commun.*, 2015, **51**, 1922–1925.

49 G. Karkera, T. Sarkar, M. Dixit Bharadwaj and A. S. Prakash, Design and Development of Efficient Bifunctional Catalysts by Tuning the Electronic Properties of Cobalt–Manganese Tungstate for Oxygen Reduction and Evolution Reactions, *ChemCatChem*, 2017, **9**, 3681–3690.

50 A. Rebekah, E. Ashok Kumar, C. Viswanathan and N. Ponpandian, Effect of cation substitution in $MnCo_2O_4$ spinel anchored over rGO for enhancing the electrocatalytic activity towards oxygen evolution reaction (OER), *Int. J. Hydrogen Energy*, 2020, **45**, 6391–6640.

51 A. Rebekah, S. Anantharaj, C. Viswanthan and N. Ponpandian, Zn-substituted $MnCo_2O_4$ nanostructure anchored over rGO for boosting the electrocatalytic performance towards methanol oxidation and oxygen evolution reaction (OER), *Int. J. Hydrogen Energy*, 2020, **45**, 14713–14727.

52 S. Anantharaj and S. Noda, Appropriate Use of Electrochemical Impedance Spectroscopy in Water Splitting Electrocatalysis, *ChemElectroChem*, 2020, **7**, 10.

53 S. Anantharaj, P. E. Karthik and S. Noda, Petal-Like Hierarchical Array of Ultrathin $Ni(OH)_2$ Nanosheets Decorated with $Ni(OH)_2$ Nanoburls: An Highly Efficient OER Electrocatalyst, *Catal. Sci. Technol.*, 2017, **7**, 882–893.

54 A. T. Swesi, J. Masud and M. Nath, Nickel selenide as a high-efficiency catalyst for oxygen evolution reaction, *Energy Environ. Sci.*, 2016, **9**, 1771.

55 M. Yang, Y. Li, Y. Yu, X. Liu, Z. Shi and Y. Xing, Self-Assembly of Three-Dimensional Zinc-Doped $NiCo_2O_4$ as Efficient Electrocatalysts for Oxygen Evolution Reaction, *Chem.–Eur. J.*, 2018, **24**, 13002–13008.

56 C. Broicher, F. Zeng, J. Artz, H. Hartmann, A. Besmehn, S. Palkovits and R. Palkovits, Facile synthesis of mesoporous nickel cobalt oxide for OER – insight into intrinsic electrocatalytic activity, *ChemCatChem*, 2019, **11**, 412–416.

57 J. Wang, T. Qiu, X. Chen, Y. Lu and W. Yang, Hierarchical hollow urchin-like $NiCo_2O_4$ nanomaterial as electrocatalyst for oxygen evolution reaction in alkaline medium, *J. Power Sources*, 2014, **268**, 341–348.

58 S. Wu, J. Liu, B. Cui, Y. Li, Y. Liu, B. Hu, L. He, M. Wang, Z. Zhang, K. Tian and Y. Song, Fluorine-doped nickel cobalt oxide spinel as efficiently bifunctional catalyst for overall water splitting, *Electrochim. Acta*, 2019, **299**, 231–244.

59 S. Chen and S.-Z. Qiao, Hierarchically Porous Nitrogen-Doped Graphene–$NiCo_2O_4$ Hybrid Paper as an Advanced Electrocatalytic Water-Splitting Material, *ACS Nano*, 2013, **711**, 10190–10196.

60 H. Hu, B. Guan, B. Xia and X. Wen (David) Lou, Designed Formation of Co_3O_4/$NiCo_2O_4$ Double-Shelled Nanocages with Enhanced Pseudocapacitive and Electrocatalytic Properties, *J. Am. Chem. Soc.*, 2015, **137**, 5590–5595.

61 C. Mahala and M. Basu, Nanosheets of $NiCo_2O_4$/NiO as Efficient and Stable Electrocatalyst for Oxygen Evolution Reaction, *ACS Omega*, 2017, **2**, 7559–7567.

62 Z. Zheng, X. Du, Y. Wang, C. M. Li and T. Qi, Efficient and Stable $NiCo_2O_4$/VN Nanoparticle Catalyst for Electrochemical Water Oxidation, *ACS Sustainable Chem. Eng.*, 2018, **6**, 11473–11479.

63 D. Zhao, M. Dai, H. Liu, L. Xiao, X. Wu and H. Xia, Constructing High Performance Hybrid Battery and Electrocatalyst by Heterostructured $NiCo_2O_4$@NiWS Nanosheets, *Cryst. Growth Des.*, 2019, **19**, 1921–1929.

64 R. P. Antony, A. K. Satpati and B. N. Jagatap, Performance of MOF-Derived Spinel Type $Ni_xCo_{3-x}O_{4-y}$ Nanocages in Efficient Methanol Electro-Oxidation, *ChemElectroChem*, 2017, **4**, 1–9.

65 Z. Li, R. Yang, B. Li, Y. Mei, D. Li, H. Wang and Q. Li, Controllable synthesis of graphene/$NiCo_2O_4$ three-dimensional mesoporous electrocatalysts for efficient methanol oxidation reaction, *Electrochim. Acta*, 2017, **252**, 180–191.

66 D. Wu, Y. Wei, X. Ren, X. Ji, Y. Liu, X. Guo, Z. Liu, A. M. Asiri, Q. Wei and X. Sun, $Co(OH)_2$ Nanoparticle-Encapsulating Conductive Nanowires Array: Room-Temperature Electrochemical Preparation for High-Performance Water Oxidation Electrocatalysis, *Adv. Mater.*, 2018, 1705366.

67 W. Lu, T. Liu, L. Xie, C. Tang, D. Liu, S. Hao, F. Qu, G. Du, Y. Ma, A. M. Asiri and X. Sun, In Situ Derived Co-B Nanoarray: A High-Efficiency and Durable 3D Bifunctional Electrocatalyst for Overall Alkaline Water Splitting, *Small*, 2017, 1700805.